A&A 447, 1093–1109 (2006)
DOI: 10.1051/0004-6361:20053728

Astronomy & Astrophysics

2D non-LTE modeling for axi-symmetric winds

II. A short characteristic solution for radiative transfer in rotating winds

J. Zsargó, D. J. Hillier, and L. N. Georgiev⋆

Dept. of Physics and Astronomy, University of Pittsburgh, 3941 O'Hara St., Pittsburgh, PA 15260, USA
e-mail: jzsargo@astro.phyast.pitt.edu

Received 30 June 2005 / Accepted 4 October 2005

ABSTRACT

We present a new radiative transfer code for axi-symmetric stellar atmospheres and compare test results against 1D and 2D models with and without velocity fields. The code uses the short characteristic method with modifications to handle axi-symmetric and non-monotonic 3D wind velocities, and allows for distributed calculations. The formal solution along a characteristic is evaluated with a resolution that is proportional to the velocity gradient along the characteristic. This allows us to accurately map the variation of the opacities and emissivities as a function of frequency and spatial coordinates, but avoids unnecessary work in low velocity regions. We represent a characteristic with an impact-parameter vector $\boldsymbol{p}$ (a vector that is normal to the plane containing the characteristic and the origin) rather than the traditional unit vector in the direction of the ray. The code calculates the incoming intensities for the characteristics by a single latitudinal interpolation without any further interpolation in the radiation angles. Using this representation also provides a venue for distributed calculations since the radiative transfer can be done independently for each $\boldsymbol{p}$.

Key words. radiative transfer – stars: early-type – stars: atmospheres – stars: mass-loss

1. Introduction

Massive stars and their winds play an important role in shaping the dynamical structure and energy budget of galaxies. For example, they enrich the ISM with nuclear processed material and deposit large amounts of mechanical energy into their surroundings. Despite decades of research and considerable advancements in our understanding of stellar envelopes, there is still much to learn. Because of the complexities of these systems, and the increasing emphasis on the details, it has become very difficult to proceed without complex numerical simulations. It is not surprising, therefore, that the history of stellar studies reflects not only our advancing knowledge but also our increasing computational capabilities. Initially, simple plane-parallel LTE models were utilized in numerical simulations (see e.g., Kurucz 1991, and references therein) and these were adequate for stars with dense atmospheres and low mass-loss rates. These models were also the only simulations that were viable on the computing facilities of the time. Unfortunately, the above simplifications cannot be extended to most early-type stars. Auer & Mihalas (1972, 1973), for example, demonstrated that the assumption of LTE is invalid in O-type stars and the statistical equilibrium equations need to be solved for the level populations. For massive stars with extensive mass-loss (e.g., Wolf-Rayet stars) geometrical effects are also important and plane-parallel models are no longer sufficient. As a minimum, therefore, one needs to use non-LTE spherical models to understand these objects. The system of statistical equilibrium equations, however, is highly non-linear in the level populations and finding a solution for fully line blanketed models is a formidable task. We have reached the necessary level in computing power only in the last few years to be able to routinely perform such computations (see e.g., Hubeny & Lanz 1995; Hauschildt et al. 1996; Hillier & Miller 1998; Pauldrach et al. 2001; Gräfener et al. 2002).

Plane-parallel and spherical non-LTE modeling have found wide applicability in spectroscopic studies. Recent works by Martins et al. (2002); Crowther et al. (2002); Hillier et al. (2003); Herrero et al. (2002) have revised the temperature scale for O stars, for example, and have given new insights into the structure of stellar winds. However, spherical (or plane-parallel) modeling also has its limitations and cannot be used to study many important stellar objects.

It has been known for a long time that some circumstellar envelopes are non-spherical – the most well-known examples are the envelopes of Be stars. The hydrogen emission and infrared excess of these stars are thought to be produced in a thin disk. The presence of these disks was inferred from both line modeling and polarimetric studies

⋆ *Present Address:* Instituto de Astronomia, Universidad Nacional Autonoma de Mexico (UNAM), CD. Universitaria, Apartado Postal 70-264, 04510, México DF, México.

(Poeckert & Marlborough 1978a,b), and has been confirmed by interferometric observations (Stee et al. 1995; Quirrenbach et al. 1997). Furthermore, recent MHD simulations (Cassinelli et al. 2002; ud-Doula & Owocki 2002; Owocki & ud-Doula 2004) argue for equatorial confinement by magnetic field for the origin of the disks. If a dynamically important magnetic field is present in Be envelopes that in itself ensures at least a 2D nature of their wind.

Other stellar problems for which 1D models are inadequate include rapidly rotating OB stars, binaries with colliding winds or accretion disks, pre-main sequence and young stars, stellar envelopes irradiated by external sources (e.g., massive stars near an AGN), and the collapsing core (Type-II) supernovae (e.g., Wang et al. 2001; Kifonidis et al. 2003). Advanced supernovae models may even have cosmological applications since these luminous objects can be used as distance calibrators in the nearby universe (see Dessart & Hillier 2005a,b, and references therein).

The case of rapid OB rotators is particularly important for this paper since we test our code on such a problem. These stars are subjects of intense research and the exact structure of the rotating envelope is not well established. The conservation of angular momentum in the wind may result in meridional flow toward the equator which potentially leads to disk formation (see e.g., Bjorkman & Cassinelli 1993). Conversely the latitudinal variation of the surface gravity will result in a variation of the radiative flux with latitude that can inhibit disk formation, and can cause a strong polar wind (Owocki et al. 1996; Maeder & Meynet 2000). Either way, the underlying spherical symmetry of the outflow is broken and at least axi-symmetric models are needed for spectral analysis.

Motivated by the need for 2D model atmospheres, and by the availability of fast computers and methods, we undertook a project to develop a tool for spectroscopic analysis of axi-symmetric stellar envelopes. The solution of the statistical equilibrium equations for the level populations and temperature is discussed in the first paper of this series (Georgiev et al. 2005, Paper I). At present the main code, ASTAROTH, solves for the radiation field by a continuum transfer routine that is based on the method of Busche & Hillier (2000) and uses the Sobolev approximation for line transfer. In this paper we present an alternate routine for ASTAROTH that can handle the line-transfer without the use of Sobolev approximation in models with continuous, but not necessarily monotonic, velocity fields. We treated this problem independently from the main project because it required experimentation with alternate solution methods. In Sect. 2 we describe our goals and motivations in finding the proper solution method, and we also give a brief discussion of the chosen approach. The C++ code that was developed for the transfer is described in Sect. 3 where we also present the test results and verification. Finally, we draw our conclusions in Sect. 4.

2. Description of the solution technique

A non-LTE model of a stellar envelope is a complex nonlinear problem. The level populations and the radiation field are strongly coupled. Thus, an iterative procedure is needed to achieve a consistent solution. To solve the statistical equilibrium equations for the level populations, one must determine the radiative transition rates for free-free, bound-free and bound-bound transitions. These require the knowledge of the radiation moments

$$J(\boldsymbol{r}, \nu) = \frac{1}{4\pi} \int_{\Omega} I(\boldsymbol{r}, \underline{\boldsymbol{n}}, \nu)\, \mathrm{d}\Omega \tag{1}$$

and

$$\overline{J}_l(\boldsymbol{r}) = \frac{1}{4\pi} \int_{\Omega} \int_{0}^{\infty} I(\boldsymbol{r}, \underline{\boldsymbol{n}}, \nu) \Phi_l(\nu)\, \mathrm{d}\nu \mathrm{d}\Omega. \tag{2}$$

The quantities $I(\boldsymbol{r}, \underline{\boldsymbol{n}}, \nu)$, $\boldsymbol{r}$, and $\underline{\boldsymbol{n}}$ are the specific intensity, the spatial position, and the direction in which the radiation is propagating, respectively. The function Φ_l represents the normalized line-profile for any given bound-bound transition and the integrations are over all solid angles and frequencies.

Only J and $\overline{J}_l$ are needed to solve the statistical equilibrium equations, but they have to be updated every iteration cycle. This introduces stringent requirements on numerical efficiency and speed, but also allows for simplifications. The Radiative Transfer (RT) code does not have to produce the observed spectrum, for example, since it is irrelevant for the transition rates. Nor do the specific intensities at each depth need to be stored. On the other hand, the run time characteristics of the code are critical for its application in an iterative procedure. Therefore, our RT code is optimized to calculate J, $\overline{J}_l$, and the "approximate lambda operator" (Λ^*, see Sect. 2.3) as efficiently as possible. Crude spectra in the observer's frame are calculated only if requested, and only for monitoring the behavior of the code.

At a minimum, a realistic non-LTE and line-blanketed model atmosphere requires the inclusion of most H, He, C, N, O, and a large fraction of Fe transitions in the calculation. The running time and memory requirements of such a model can be several orders of magnitude larger in 2D than those of its spherical or plane-parallel counterpart. The dramatic increase in computational effort arises from both the extra spatial dimension, and from the extra variable needed to describe the angular variation of the radiation field. In spherical models, for example, the radiation field is symmetric around the radial direction – a symmetry which is lost in 2D. We believe that realistic 2D/3D simulations, especially in the presence of non-monotonic flow velocities, will inevitably require the simultaneous use of multiple processors. Therefore, we developed ASTAROTH and this RT code to be suitable for distributed calculations by ensuring that their sub-tasks are as independent from each other as possible.

2.1. The solution of the radiative transfer

Our choice to calculate moments J and $\overline{J}_l$ is to solve the radiative transfer equation for static and non-relativistic media

$$\underline{\boldsymbol{n}} \boldsymbol{\nabla} I(\boldsymbol{r}, \underline{\boldsymbol{n}}, \nu) = -\chi(\boldsymbol{r}, \underline{\boldsymbol{n}}, \nu) \left[I(\boldsymbol{r}, \underline{\boldsymbol{n}}, \nu) - S(\boldsymbol{r}, \underline{\boldsymbol{n}}, \nu) \right], \tag{3}$$

and then evaluate the integrals in Eqs. (1) and (2). The quantities χ and S in Eq. (3) are the opacity and source function, respectively. A major simplification in this approach is that a formal solution exists for Eq. (3). At any s position along a

given ray (or characteristic), the optical depth and the specific intensity are

$$\tau_\nu = \int_0^s \chi \mathrm{d}s' \tag{4}$$

and

$$I(\tau_\nu) = I_{\rm BC}\, \mathrm{e}^{-\tau_\nu} \; + \; \int_0^{\tau_\nu} S(\tau')\, \mathrm{e}^{\tau'-\tau_\nu}\, \mathrm{d}\tau', \tag{5}$$

respectively (from now on, we stop indicating functional dependence of quantities on $\boldsymbol{r}$, $\underline{\boldsymbol{n}}$, and ν). Therefore, the intensity can be calculated by specifying $I_{\rm BC}$ at the up-stream end ($s = 0$) of the ray and by evaluating two integrals (assuming that S and χ are known). We sample the radiation field by a number of rays for every spatial point. If the number and the orientation of the rays are chosen properly, then the angular variation of I is sufficiently reproduced and accurate J and $\overline{J}_l$ can be calculated.

There are alternatives to this simple approach; each has its own merits and drawbacks. For example, from Eq. (3) one can derive differential equations for the moments of the radiation field and solve for them directly. This approach has been successfully used in 1D codes, like CMFGEN (Hillier & Miller 1998), and in calculations for 2D continuum/grey problems (Busche 2001). A distinct advantage of the method is that electron scattering (ES) is explicitly included in the equations, and consequently no ES iteration is needed. However, to achieve a closed system of moment equations a closure relationship between the various moments is required. This relationship is generally derived from the formal solution which requires at least a fast and rudimentary evaluation of Eqs. (4) and (5). Furthermore, the 2D moment equations are quite complicated and it is not easy to formulate the proper boundary conditions in the presence of non-monotonic velocity fields. For our purposes we needed a simple approach that is flexible enough to implement in distributed calculations.

An increasingly popular method to solve the RT is using Monte-Carlo simulations. In this method, a large number of photon packets are followed through the envelope and the properties of the radiation field are estimated by using this photon ensemble (see e.g., Lucy 1999, 2002, 2003). While the Monte-Carlo simulations are flexible and suitable for parallel computing, they can also have undesirable run-time characteristics. It is also unclear how line overlaps in the presence of a non-monotonic velocity field can be treated by Monte-Carlo techniques without the use of Sobolev approximation.

After considering our needs and options, we decided to use the straightforward approach, solving Eq. (3) and evaluating Eqs. (1) and (2). This approach provides a reasonable compromise of accuracy, numerical efficiency, and flexibility. Our code will also increase the pool of available RT programs in stellar studies. Each solution technique has its specific strength (e.g., our method is fast enough for an iterative procedure) and weaknesses; therefore, future researchers will have more options to choose the best method for their needs. Having a selection of RT codes that are based on different solution methods will also allow for appropriate cross-checking of newly developed programs.

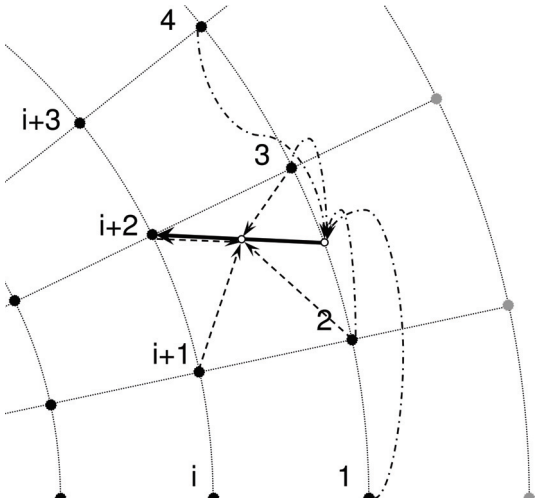

Fig. 1. A sub-section of a typical spatial grid used in our RT code. The boundary and internal points are indicated by grey and black dots, respectively. The solid arrow represents a SC belonging to point $i+2$ and pointing in the direction of the radiation. Note, that the characteristic is terminated at the closest cell boundary (between nodes 2 and 3), and is not followed all the way to the boundary of the domain (grey points). The numbering at the nodes indicates the order in which the intensity in this direction is evaluated. The small empty circles on the SC are the integration points (see Sect. 2.1) and the dashed arrows show which grid points are used for interpolating χ and S (straight arrows), or $I_{\rm BC}$ (curved arrows).

The most accurate solutions for Eqs. (4) and (5) are achieved when the integrals are evaluated all the way to the boundary of the modeling domain along each ray (Long Characteristic (LC) method, Jones 1973; Jones & Skumanich 1973). To increase efficiency, we decided to use the so-called "Short-Characteristic" (SC) method, first explored by Mihalas et al. (1978) and Kunasz & Auer (1988). In our implementation of this method, the characteristics are terminated at the next up-stream radial shell (normally, they would be terminated at any cell boundary) where $I_{\rm BC}$ is calculated by an interpolation between the specific intensities of the nearest latitudinal grid points (see Fig. 1). We calculate the specific intensity in a given direction for all grid points starting with those at the upstream end of the domain (where I is set to the appropriate boundary condition) and proceed with the calculation downstream (see Fig. 1 for details). This evaluation scheme ensures that all intensity values are calculated by the time they are needed for the interpolation of $I_{\rm BC}$. With this simple trick, the specific intensity is calculated very efficiently but for the cost of introducing coupling between the directional sampling of the intensity at the grid points. We will discuss the implications of this coupling in Sect. 2.2.

On every SC, we evaluate the integrals of Eqs. (4) and (5) for every co-moving frequency of the down-stream end point ($i + 2$ in Fig. 1) by

$$\tau = \sum_{j=1}^{N-1} \Delta\tau_j \qquad \Delta\tau_j = \frac{\chi_{j+1} + \chi_j}{2}(s_{j+1} - s_j) \tag{6}$$

and

$$\int_0^{\tau_\nu} S(\tau')\mathrm{e}^{\tau'-\tau_\nu}\,\mathrm{d}\tau' = \sum_{j=1}^{N-1}\frac{S_{j+1}}{\Delta\tau_j}\left(\Delta\tau_j + \mathrm{e}^{-\Delta\tau_j} - 1\right) - \sum_{j=1}^{N-1}\frac{S_j}{\Delta\tau_j}\left(\Delta\tau_j + \left(1+\Delta\tau_j\right)\left(\mathrm{e}^{-\Delta\tau_j}-1\right)\right) \quad (7)$$

where $N-1$ is the number of integration steps. Eqs. (6) and (7) can be easily derived from Eqs. (4) and (5) by assuming that in each interval χ and S are linear in s and τ, respectively. To ensure that the spatial and frequency variations of the opacity and source function are mapped properly, we divide the SC into small $s_{j+1} - s_j$ intervals by placing enough "integration" points on the characteristic. The number of these points (N) depends on the ratio of the "maximum line of sight velocity difference" along the SC and an adjustable "maximum allowed velocity difference". By choosing this free parameter properly we ensure adequate frequency mapping but avoid unnecessary calculations in low velocity regions. Further, we can trade accuracy for speed at the early stages of the iteration and later "slow down" for accuracy. We allowed for 20 km s^{-1} velocity differences along any SC in the calculations that we present here. Even though this is larger than the average frequency resolution of our opacity and emissivity data (~10 km s^{-1}), it was still adequate. Trial runs with 2 km s^{-1} and 20 km s^{-1} "maximum allowed velocity difference" for the 1D model with realistic wind velocities (see Sect. 3.2) produced nearly identical results.

The line of sight velocities, χ_j, and S_j are calculated at the integration points by bi-linear interpolations using the four closest spatial grid points (see Appendix A and Fig. 1). We would like to emphasize, that the interpolated χ_j and S_j are in the co-moving frame and not in the frame in which the integration is performed. This difference must be taken into account in Eqs. (6) and (7) by applying the proper Doppler shifts at each integration point (see Appendix A).

With the exception of the intensity, all quantities are interpolated assuming that they vary linearly between nodes. Extensive testing of our code revealed that at least a third-order interpolation is necessary to calculate $I_{\rm BC}$ sufficiently accurately (see Appendix A.2). For all other quantities first-order approximation is adequate in most cases but not in all. Since we wished to keep the first-order approximations if possible (it is the least time consuming and is numerically well behaved), a simple multi-grid approach was introduced to improve accuracy. Unlike the intensity calculation, the interpolation of χ and S *do not* have to be performed on the main grid; therefore, a dense spatial grid for opacities and source functions can be created, using monotonic cubic interpolation (Steffen 1990), before the start of the calculation. Then, we use this dense grid to perform the bi-linear interpolations to the integration points but perform the RT calculation only for spatial points on the main grid. Before the next iteration, the opacities and source terms on the dense grid are updated. To ensure a straightforward Λ^* calculation we require the main grid to be a sub-grid of the dense grid. Further, the use of the dense grid is optional and only required if more accurate approximations of χ and S are desired. With this rudimentary multi-grid technique, we improved the accuracy of our calculations for essentially no cost in running time (~5–10% increase). However, there was a substantial increase in memory requirement. To avoid depleting the available memory, the RT is usually performed in frequency batches that can be tailored to fit into the available memory. This technique not only decreases the memory requirements, but also provides an excellent opportunity for parallelization.

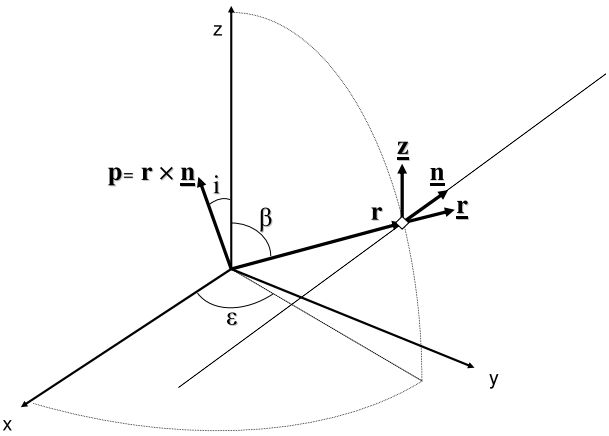

Fig. 2. The definition of our fundamental coordinate system. The unit vector $\underline{\boldsymbol{n}}$ describes a characteristic (long thin line) pointing in the direction of the radiation and r, β, and ϵ are the traditional polar coordinates of a spatial point. Note that it is assumed here and in the rest of the paper that z axis is the axis of symmetry. We use the impact-parameter vector $\boldsymbol{p}$ (which is perpendicular to the plane containing the characteristic and the origin), instead of $\underline{\boldsymbol{n}}$, to represent a particular characteristic (see Sect. 2.2 for explanations).

2.2. Our coordinate system and representation of directions

Most 2D problems that we are going to treat are "near-spherical" with a moderate departure from a general spherical symmetry. The radiation field is usually dominated by a central source in these cases, and it is practical to treat them in a spherical coordinate system. Therefore, we decided to use r, β, and ϵ (see Fig. 2 for definition) for reference in our code.

In spherical symmetry, the most natural way to map the directional variation of the intensity is using the "so-called" radiation coordinates, θ and ϕ, that are defined by

$$\cos(\theta) = \underline{\boldsymbol{n}} \cdot \underline{\boldsymbol{r}} \quad (8)$$

and

$$\sin(\theta)\cdot\sin(\beta)\cdot\cos(\phi) = \left[\underline{\boldsymbol{n}}\times\underline{\boldsymbol{r}}\right]\cdot\left[\underline{\boldsymbol{r}}\times\underline{\boldsymbol{z}}\right]. \quad (9)$$

The unit vectors $\underline{\boldsymbol{n}}$, $\underline{\boldsymbol{r}}$, and $\underline{\boldsymbol{z}}$ are pointing in the direction of the radiation, in the radial direction, and in the positive side of the z axis, respectively (see Fig. 2). A proper choice of θ angle grid can be very useful in treating inherent discontinuities around the limb of the central star and the symmetries due to the forward-peaking nature of the radiation field.

As mentioned in Sect. 2.1 a serious drawback of the SC method is the interdependency of the specific intensities

at different grid points. Beside introducing systematic errors by the successive intensity interpolations, the SC method also couples the directional sampling of the radiation field on the grid. Our choice of directions at a grid point not only has to suit the needs of the particular point but also has to be able to provide suitable starting values ($I_{\rm BC}$) for other points. Unfortunately, θ and ϕ vary along a characteristic so it is not possible to use a uniform θ and ϕ grid for all grid points without intensity interpolations in the radiation coordinates. The later option is not desirable for multidimensional RT. First, it requires a large amount of memory to store all intensities for the interpolation. Second, it makes the parallelization of the code difficult.

To find a proper directional sampling method one needs to look for quantities that are conserved along a characteristic, like

$$\boldsymbol{p} = \boldsymbol{r} \times \underline{\boldsymbol{n}}, \tag{10}$$

which we call the "impact-parameter vector" (see Fig. 2). This vector describes all essential features of a characteristic and can be considered as an analog of the orbital momentum vector in two body problems. Its absolute value $p = |\boldsymbol{p}|$ is the traditional impact-parameter and its orientation defines the "orbital plane" of the radiation (the plane that contains the characteristic and the origin). Following this analogy one can define an "inclination" angle for this plane by

$$p \cdot \cos(i) = \boldsymbol{p} \cdot \underline{z}. \tag{11}$$

In our code we set up a universal grid in impact-parameters (p) and in inclination angles (i) for directional sampling. As opposed to the θ and ϕ angles, the inclination angle and the impact-parameter do not vary along a ray; therefore, intensities in the proper directions will be available for the interpolation when the transfer is solved for a given i and p. Using an impact-parameter grid to avoid interpolation in θ angle has already been incorporated into previous works (e.g., Busche & Hillier 2000). By introducing the inclination angle grid we simply exploited the full potential of this approach.

It is useful to examine the relationship between the radiation angles and our directional coordinates. The conversion is via

$$\sin(\theta) = \frac{p}{r} \tag{12}$$

and

$$\sin(\phi) = \frac{\cos(i)}{\sin(\beta)} \tag{13}$$

at each grid point. Equation (13) can be easily derived by spherical trigonometry as illustrated by Fig. 3. One can see from Eqs. (12) and (13) that there is a degeneracy between "incoming"–"outgoing", as well as between "equator-bound"–"pole-bound" rays. (The "pole-bound" rays are defined by $\frac{\pi}{2} < \phi < \frac{3}{2}\pi$.) The radiation coordinates (θ, ϕ) and ($\pi - \theta$, $\pi - \phi$) are represented by the same (p, i) pair. Fortunately, the "switch-over" can only occur at certain spatial positions. For example, the incoming rays become outgoing only at $r = p$, so this is just a simple book-keeping problem. Nevertheless, one should always bear this degeneracy in mind when doing the actual programming implementation of our method.

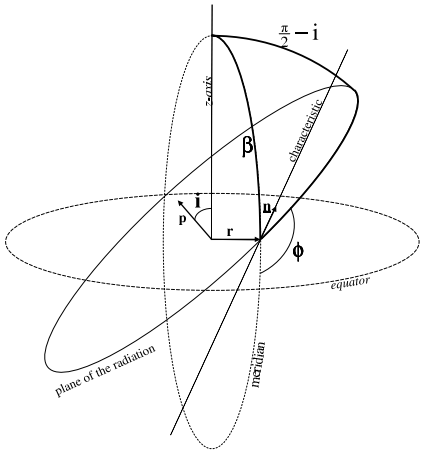

Fig. 3. Diagram illustrating the connection between the radiation angle ϕ and the inclination angle. The "plane of the radiation" includes the characteristic and the origin. Angles i and β are the angular distances between the z-axis and the directions of the $\boldsymbol{p}$ and $\boldsymbol{r}$ vectors, respectively. Equation (13) can be derived by a spherical sine law using the boldface spherical triangle.

There remains one important question. How exactly do we choose the actual impact-parameter and inclination angle grid? We adopted the approach of Busche & Hillier (2000) who used the radial grid and a number of "core rays" ($p \le r_{\rm core}$) for the impact-parameters. The core rays are added only if a central source with a radius $r_{\rm core}$ is present in the model. This will provide a radius dependent sampling since only $p \le r$ can be used for a given r radius. Also, the sampling is uneven and sparser around $\theta = \frac{\pi}{2}$ than around $\theta = 0$ or π. Nevertheless, this grid was proven to be adequate for near spherical problems and also very convenient to use. For example, it ensures that $p = r$ (the switch-over from "incoming" to "outgoing" ray) is always a grid point. Similarly, we based our inclination angle grid on the β grid, although, we have the option to define it independently. If needed, extra inclination angles can also be included around $i = \frac{\pi}{2}$ to increase the ϕ angle resolution at higher latitude.

Figure 4 illustrates a typical inclination angle grid and the ϕ-angle sampling it provides. For illustration purposes we use a hypothetical β grid of $\frac{1}{2}\pi$ (equator), $\frac{8}{10}\pi$ (72°), $\frac{6}{10}\pi$ (54°), $\frac{4}{10}\pi$ (36°), $\frac{2}{10}\pi$ (18°), and 0 (pole). Then, one may choose these β values and their corresponding complementary angles ($\pi - \beta$) for the inclination angle grid. By our definition, angles $i \le \frac{\pi}{2}$ sample the $0 \le \phi \le \pi$ range, while $i > \frac{\pi}{2}$ covers the rest of the ϕ space (see Fig. 4). The behavior of the ϕ-angle sampling created by this inclination angle grid is very similar to that of the θ-angle sampling provided by the radial grid. One can easily see from Eq. (13) that for a given β any $i < \frac{\pi}{2} - \beta$ has no solution for ϕ. The equatorial regions ($\beta \sim \frac{\pi}{2}$), therefore, are well sampled in ϕ angle while there is only one valid inclination angle at $\beta = 0$ ($i = \frac{\pi}{2}$). This is reasonable in axi-symmetrical models, as long as the polar direction is also the axis of symmetry (as we explicitly assume). The ϕ-angle sampling is also uneven. The regions around $\phi = 0$ and π (local meridian) are better resolved than those around $\phi = \frac{\pi}{2}$ and $\phi = \frac{3}{2}\pi$. In Sects. 3.1–3.3 we will

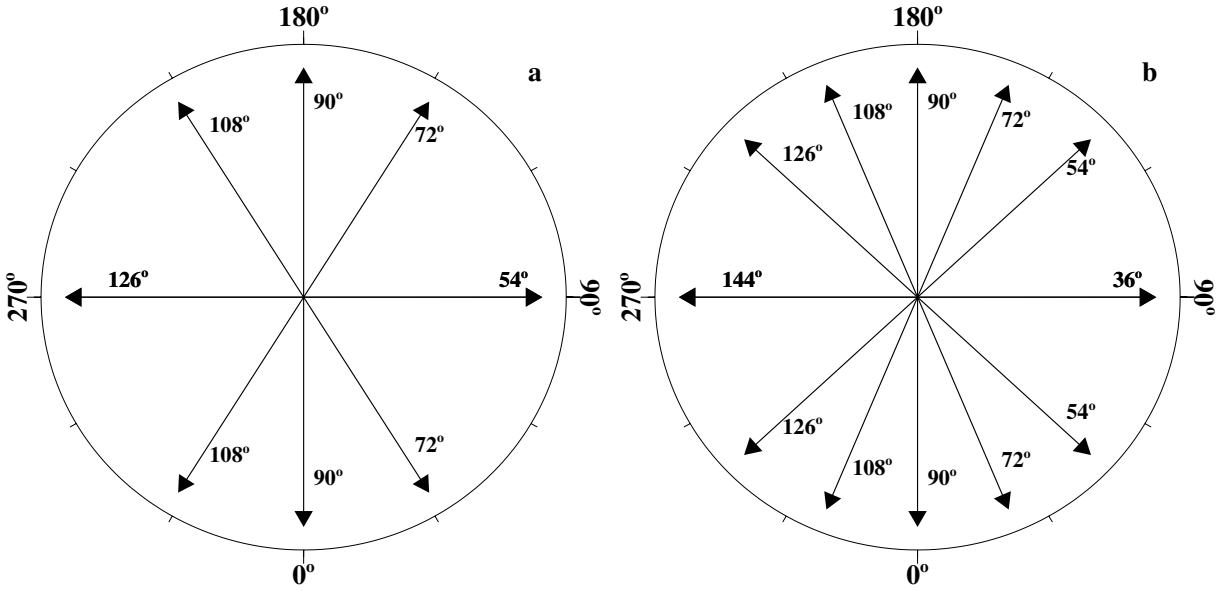

Fig. 4. The ϕ-angle plane at different latitudes as viewed by an observer facing the central star/object. The unit vector pointing out of the page is toward the observer. Each figure is centered on the line of sight of the observer and the equator is toward the bottom of the page. The figure was created for inclination angles of 0°, 18°, 36°, 54°, 72°, 90°, 108°, 126°, 144°, 162°, and 180° which are indicated near the head of the arrows. The radiation angle ϕ is measured counter-clockwise from the direction toward the equator as indicated on the outer rim of the circles. Panels a and b are for $\beta = 36°$ and 54°, respectively. For clarity, we assumed that the impact-parameter (p) of the rays is equal to r; therefore, any direction that we sample lies in the ϕ plane. The figure shows that the ϕ-angle coverage is latitude dependent and unevenly spaced. Note, for example, the absence of $i = 0°$, 18°, 36° (and their complementary angles) for $\beta = 36°$.

demonstrate that our sampling method not only eliminates the need for interpolations in θ and ϕ angles, but sufficiently recovers the directional variation of the radiation at every point and is adequate for RT calculations in axi-symmetric envelopes.

2.3. Approximate Lambda Iteration

A seemingly natural choice for the iteration between the RT and level populations is the notorious "Λ-iteration". In this scheme, the level populations from the previous cycle are used to calculate new J and $\overline{J}_l$ which in turn are used to update the populations. Unfortunately, this simple procedure fails to converge for large optical depths. Convergence is ensured, however, by using the Accelerated Lambda Iteration (ALI; see e.g., Rybicki & Hummer 1991; Hubeny 1992) which takes some of the inherent coupling into account implicitly. The relationship between J and the source function S can be summarized as

$$J = \Lambda\,[S]\,, \tag{14}$$

where the Λ operator can be derived from Eqs. (1) and (3). Both Λ operator and S depend on the level populations, however, we can "precondition" Λ (i.e., use the populations from the previous cycle to evaluate it, see e.g., Rybicki & Hummer 1991) and only take the coupling through S into account to accelerate the iteration. In 2D, Λ in its entirety is too complicated to construct and time consuming to invert, which is necessary to take the coupling into account. We can, however, split the Λ operator into an "easy-to-invert" Λ^* (Approximate Lambda Operator) and the remaining "difficult" part by

$$J = \Lambda^*\,[S]\; + (\Lambda - \Lambda^*)\,[S]\,. \tag{15}$$

Then, we can precondition the "difficult" part by using the old populations, and accelerate the iteration by inverting Λ^*. Note, that the full Λ operator never needs to be constructed, only Λ^* since

$$(\Lambda - \Lambda^*)\left[S^{i-1}\right] = J^{i-1} \;-\; \Lambda^*\left[S^{i-1}\right] \tag{16}$$

where J^{i-1} and S^{i-1} is the moment and source term from the previous iteration cycle.

The actual form of Λ^* is a matter of choice as long as it can be easily inverted. The most practical in 2D is separating out the local contribution (i.e., diagonal part of the Λ operator when written in a matrix form). This is easy to calculate and has reasonably good convergence characteristics. During the evaluation of moments J and J_l (see Sect. 2.1), we also calculate the diagonal Λ^* operator. This is a fairly straightforward bookkeeping since we just have to add up the weights used for the local source function during the integration of Eq. (5).

We used the Λ^* operator to accelerate the ES iterations in our test calculations (see the following sections). Apart from the initial "hiccups" of code development, the operator always worked as expected and produced the published convergence characteristics (Rybicki & Hummer 1991). The implementation of the ALO iteration into the solution of the statistical equilibrium equation is discussed in Paper I.

3. Code verification and test results

We have developed a C++ code that implements the solution technique described in Sect. 2. As mentioned in Sect. 2.1, we used a modified version of the traditional SC method by terminating the characteristics at the closest spherical shell rather

than any cell boundary (i.e., our SCs cross cell boundaries in β direction). This modification allows us to avoid intensity interpolations in the radial direction which increases the accuracy when a strong central source dominates the radiation field. The transfer calculation for an impact-parameter (p) and inclination angle (i) pair is performed on an axi-symmetric torus with an opening-angle of $2i$ and which is truncated at the inner radius of $r = \max(p, r_{\rm core})$. This torus contains all spatial regions that a ray described by p and i can reach. The calculation starts at the outermost radius and proceeds inward, shell by shell, until the truncation radius is reached; then, the outgoing radiation is calculated in a similar manner by proceeding outward. At the outer boundary we set the incoming intensity to zero while either a diffusion approximation or a Schuster-type boundary condition can be used at the truncation radius if it is equal to $r_{\rm core}$. In its present form, the code assumes top-bottom symmetry, however, this approximation can easily be relaxed to accommodate general axi-symmetric models. The RT calculation for each (p, i) pair is independent from any other. The only information they share are the hydrodynamic structure of the envelope, the opacities, and emissivities; all of which can be provided by ASTAROTH.

There are at least two major venues to accommodate multiprocessor calculations in the code. One way is to distribute the (p, i) pairs among the available processors. To optimize the calculation one needs to resolve a non-trivial load-sharing issue. The actual number of spatial grid points involved in the RT is not the same for all (p, i) pairs, so the duration of these calculations is not uniform. For example, the transfer for $p = 0$ and $i = \frac{\pi}{2}$ involves all spatial grid points, while the one for $p = 0$ and $i = 0$ includes only the points lying in the equator. To use the full capacity of all processors at all times, a proper distribution mechanism needs to be developed that allows for the differences between processors and the differences between (p, i) pairs.

We also have the option to distribute the work among the processors by distributing the frequencies for which the RT is calculated. In this case, the work-load scales linearly with the number of frequencies, so the distribution is straightforward. However, the lack of sufficient memory may prevent the distribution of all opacities and emissivities and the processors may have information only over their own frequency range. To take the effects of velocity field into account at the limiting frequencies, we introduce overlaps between the frequency regions.

So far, we have performed multi-machine calculations where the (p, i) pairs or frequency ranges were distributed by hand. The results of the distributed calculations were identical to those performed on a single machine. Work is under way to fully implement distributed calculations by using MPI protocols. Since our goal is to run the entire stellar atmosphere code on multiple processors, we will discuss the details of parallelization in a subsequent paper after we have fully integrated our code into ASTAROTH.

In the following we describe the results of some basic tests of our code. First, we calculate the radiation field in static 2D problems with and without ES. Then, we present our results for realistic spherical problems with substantial wind velocities. Finally, we introduce rotation in a spherical model and demonstrate the ability of our code to handle 2D velocity fields.

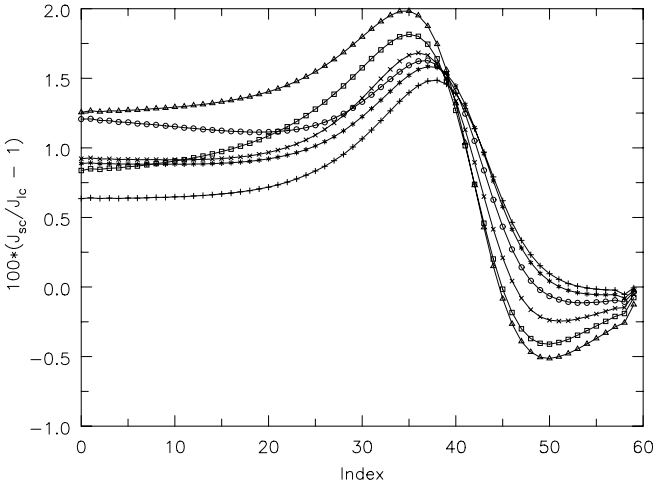

Fig. 5. The percentage difference between the J moments calculated by our ($J_{\rm sc}$) and by the LC program ($J_{\rm lc}$) as a function of the depth index (0 and 59 are the indices of the outer-most and inner-most radial grid points, respectively) for different latitudes. The ES opacity in this model is described by Eq. (17). The symbols +, *, o, ×, □, and △ indicate the differences for $\beta = 0$, 0.1π, 0.2π, 0.3π, 0.4π, and $\frac{\pi}{2}$, respectively. Our code systematically overestimates J in the outer regions (0−40) which is mostly due to the second order accuracy of the radial interpolations. Errors from other sources (e.g., latitudinal resolution, ϕ angle sampling) are most important at high-latitudes ($\beta \sim 0.1$−$0.2\,\pi$) but still contribute less than ∼1%.

3.1. Static 2D models

The basic characteristics of our code were tested by performing simple calculations, 1D and 2D models without velocity field. We used the results of a LC program developed by Hillier (1994, 1996) as a benchmark. This code was extensively tested and verified by reproducing one dimensional models as well as analytical solutions available for optically thin stellar envelopes (e.g., Brown & McLean 1977). It was also tested against Monte-Carlo simulations of more complicated models.

Our code reproduced the results of the LC program within a few percent for all spherical and axi-symmetric models. It was proven to be very stable and was able to handle extreme cases with large optical depths. The most stringent tests were the transfer calculations in purely scattering atmospheres. In such cases, the necessary iterations accumulate the systematic errors which highlights any weakness in the program. Several 1D and 2D scattering models were run with ES optical depths varying between 1 and 100. Figures 5 and 6 compare our results to those of the LC code for a model with electron scattering opacity distribution of

$$\chi_{\rm es} = 10 \cdot \left[\frac{r_{\rm core}}{r}\right]^3 \cdot \left(1 - \frac{1}{2} \cdot \cos^2\beta\right). \quad (17)$$

No other source of opacity and emissivity was present in the model. At the stellar surface we employed a Schuster-type boundary condition of $I_{\rm BC} = 1$, while $I_{\rm BC} = 0$ was used at the outer boundary. The ES iteration was terminated when

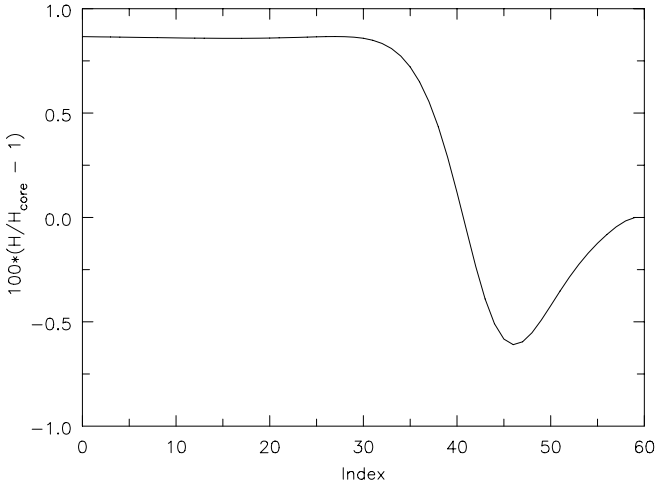

Fig. 6. The percentage loss/gain of the total radial flux ($H = \int_{4\pi} H_r r^2 \mathrm{d}\Omega$) with respect to the total flux emanating from the stellar surface (H_{core}) as a function of depth index for the 2D model described by Eq. (17). The flux is conserved within ∼1%.

$\frac{\Delta J}{J} \leq 0.001\%$ had been achieved. This model is an ideal test case since the ES optical depth is large enough to require a substantial number of iterations to converge, but the convergence is fast enough to allow for experimenting with different spatial resolutions.

For the results we present in Fig. 5, the LC code was run with 60 radial and 11 latitudinal grid points. The ϕ radiation angle was sampled in 11 directions evenly distributed between 0 and π. This code assumes top-bottom and left-right symmetry around the equator ($\beta = \frac{\pi}{2}$) and the local meridian ($\phi = 0$), respectively, so only half of the β and ϕ space had to be sampled. The radial grid, supplemented by 14 core rays, was used to map the θ radiation angle dependence (see Sect. 2.2 for description). We used a slightly modified radial and latitudinal grid in our code. We added 3 extra radial points between the 2 innermost depths of the original grid, and 6 extra latitudinal points were placed between $\beta = 0$ and $0.15\ \pi$. These modifications substantially improved the transfer calculation deep in the atmosphere and at high latitudes. The sampling method of the θ angle was identical to that of the LC code. We based our inclination angle grid on the β grid and added 4 extra inclination angles around $\frac{\pi}{2}$ to improve the coverage at high latitudes. This grid resulted in a latitude dependent ϕ angle sampling. At the pole, the radiation was sampled in only 2 directions while on the equator 60 angles between 0 and 2π were used. Note, that our code does not assume left-right symmetry!

Figures 5 and 6 show that we were able to reproduce the results of the LC code within ∼2% accuracy, and the total radial flux is conserved within 1% level. It is also obvious that our code needs higher spatial resolution to achieve the accuracy of the LC code. This is expected since the LC program uses higher order approximations and adds extra spatial points when needed to increase the overall accuracy. In fact, one should not call the LC code a pure $N_r = 60$, $N_\beta = 11$ model. The auxiliary points increased the real resolution. It is not surprising, on the other hand, that our code runs substantially faster on the same machine. The difference was between a factor of 10 and 2, depending on the number of iterations needed to converge. Unfortunately, we have not yet introduced sophisticated acceleration techniques, like the Ng acceleration (Ng 1974), so our code is not the most efficient when a very large number of iterations is needed.

The agreement between our code and the LC code progressively worsened as the total ES optical depth increased. Satisfactory agreement could be achieved, however, by increasing the radial resolution. Our test problems and most of the real problems that we will address later are near spherical with a modest latitudinal variation. The intensity reflects the strong radial dependency and, therefore, the radial resolution controls the overall accuracy. Figure 5 reveals another feature of our method that affects the accuracy. Our result is sensitive to the high-latitude behavior of the intensity for a given inclination angle and impact-parameter. At the high-latitude regions, a given inclination angle samples directions that can be almost parallel with the equator. Slightly different directions that are almost parallel with the equator can sample very different radiation in some axi-symmetric models, such as models with thin disks. Aggravating this problem, our method also uses fewer directions to map the radiation field at these high latitudes, unless extra inclination angles around $\frac{\pi}{2}$ are included. This explains why we had to use extra latitudes and inclination angles to produce the result for Figs. 5 and 6. We would like to emphasize, however, that these problems are important only in extreme axi-symmetric models (e.g, very thin disks or strong polar jets). Many times, as it will be demonstrated in the next sections, reasonable accuracies can be achieved on ordinary and simple grids.

During the static 2D tests, we also experimented with the multi-grid capability of our code and verified its scaling behavior. Tests with progressively increasing spatial resolution showed that our code has second order accuracy. By doubling the number of radial grid points, for example, the errors decreased roughly 4-fold. We also performed the ES iterations in multiple steps and at progressively increasing resolution. First, a coarse grid was created (e.g., half of the nominal resolution) for a crude and fast initial iteration. Then, with the updated source terms, a second iteration was performed on the nominal grid. This "double iteration" scheme was generally a factor of two faster than a single iteration on the nominal grid. This approach will be a promising venue for fast iterations in combination with other acceleration techniques.

3.2. 1D test cases with realistic wind velocities

After performing static 2D tests, we applied our code to realistic 1D atmospheres. The primary purpose of these tests was to verify our handling of realistic velocity fields. We used a well known and tested 1D stellar atmosphere code, CMFGEN (Hillier & Miller 1998), for comparison. Observed spectra for a CMFGEN model are calculated independently by an auxiliary routine, CMF_FLUX (see Busche & Hillier 2005, for a description). We compared our simulated observed spectra to those of CMF_FLUX.

Table 1. Description of model v34_36C.

Star	AV 83
Sp. type	O7 Iaf
$\log g$	3.25
R	19.6 $R_\odot$
$T_{\rm eff}$	34 000 K
$\dot{M}$	2.5×10^{-6} $M_\odot$ yr^{-1}
V_∞	900 km s^{-1}
β^a	2

[a] Power for CAK velocity law (Castor et al. 1975).

We have an extensive library of CMFGEN models to choose a benchmark for our tests. We picked AV 83, a supergiant in the SMC (see Table 1) which was involved in a recent study of O stars (Hillier et al. 2003). Accurate rotationally broadened spectra with different viewing angles are also available for this star (Busche & Hillier 2005) which we will use for comparison in Sect. 3.3. A detailed description of the CMFGEN models for AV 83 can be found in Hillier et al. (2003). We chose their model v34_36C (see Table 1) to test our code. The radial grid with 52 depth points was adopted from this model. The impact-parameter grid which samples the θ radiation angle was defined by the radial grid augmented by 15 core rays (see Sect. 2.2 for details). Our simulation was run as a real 2D case with two latitudinal angles ($\beta = 0$ and $\frac{\pi}{2}$). We used 3 inclination angles which resulted in transfer calculations for 2 and 4 ϕ angles in the polar and the equatorial directions, respectively. The RT calculations were performed on frequency regions centered around strategic lines, like Hα. A coarse grid ($N_r = 26$, $N_\beta = 2$) and the nominal ($N_r = 52$, $N_\beta = 2$) grid was used for the ES iteration as in the cases of static models (see Sect. 3.1). Note, that our model is not a fully consistent solution because we did not solve for the level populations. We simply used the output opacities and emissivities of the converged CMFGEN model and calculated the RT for it.

Figure 7 shows the normalized J moment as a function of wavelength for the C IV $\lambda\lambda$1548−1552 doublet and Hα at different depths. The results of our code and those of CMFGEN are in good agreement, except that we resolve narrow lines better. CMFGEN solves the moment equation in the co-moving frame, starting at the largest frequency. This procedure introduces bleeding which broadens the sharp lines. Our results are not affected by this bleeding since we use the formal solution.

Figure 8 shows the observed spectrum for AV 83 in the observer's frame. As is the case with the J moment the agreement between our code and CMF_FLUX is excellent. In this case CMF_FLUX does a better job but this is expected. Our code is primarily for providing J and $\overline{J}_l$ for the solution of the rate equations while it produces observed spectra only for testing. The main purpose of CMF_FLUX, on the other hand, is to produce highly accurate spectra in the observer's frame.

We would like to emphasize that our code did not need higher spatial resolution to reproduce the results of CMFGEN/CMF_FLUX, as opposed to some cases presented in Sect. 3.1. The pure scattering models of Sect. 3.1 were extreme examples and were hard to reproduce. The comparison with CMFGEN proves that our code can handle realistic problems at a reasonable spatial resolution.

3.3. Tests with a rotating envelope

As a final test for our SC code we ran simulations of semi-realistic 2D atmospheres. These were created by introducing rotation in otherwise 1D models. AV 83 offers a good opportunity for such an experiment. It has a slowly accelerating wind and low terminal velocity that enhances the importance of the rotational velocities. Also, its spectrum contains numerous photospheric and wind features which behave differently in the presence of rotation.

Capitalizing on these features Busche & Hillier (2005) used AV 83 to test their code for calculating observed spectra in 2D models, and to perform a comprehensive study of the observable rotation effects. They utilized the LC method and a very dense directional sampling to calculate the observed spectra for an arbitrary viewing angle. This code serves the same purpose for ASTAROTH as CMF_FLUX does for CMFGEN; to calculate very accurate observed spectra for an already converged model. Since our code produces observed spectra only for testing purposes and error assessment, the comparison provides only a consistency check between the two codes. Further, Busche & Hillier (2005) do not calculate radiation moments, so we could only examine whether our results behave as expected with respect to the 1D moments of CMFGEN.

The rotation in the envelope of AV 83 was introduced by using the Wind Compressed Disk model (WCD, Bjorkman & Cassinelli 1993). Busche & Hillier (2005) ran several calculations to study the different aspects of rotation. We adopted only those that were used to study the Resonance Zone Effects (RZE, Petrenz & Puls 1996). To isolate RZE-s, the latitudinal velocities were set to zero and the density was left unaffected by the rotation (i.e., it was spherical). The azimuthal velocity in such simplified WCD cases is described by

$$v_\phi = v_{\rm eq} \cdot \frac{r_{\rm core}}{r} \cdot \sin(\beta) \tag{18}$$

(see Bjorkman & Cassinelli 1993; Busche & Hillier 2005). For the maximum rotational speed on the stellar surface ($v_{\rm eq}$) we adopted 250 km s^{-1} following Busche & Hillier (2005). The radial velocity in the WCD theory is described by a CAK velocity law, so we used the same radial velocities as in Sect. 3.2.

We again adopted the radial grid of model v36_34C (Hillier et al. 2003) and used three β angles (0, $\frac{\pi}{4}$, and $\frac{\pi}{2}$). In addition to these grids we had a dense radial and latitudinal grid ($N_r = 205$, $N_\beta = 9$) for the interpolation of opacities, emissivities, and velocities; and a coarse grid ($N_r = 26$, $N_\beta = 2$) for the ES iteration. We used 14 inclination angles, evenly spaced between 0 and π, which resulted in intensity calculations for 24 ϕ angles (between 0 and 2π) at every point on the equator. As before, we performed our "double ES iteration scheme" (see Sects. 3.1 and 3.2) with convergence criteria of $\frac{\Delta J}{J} \leq 0.001\%$.

Figures 9 and 10 show the behavior of the J moment around the C IV $\lambda\lambda$1548−1552 doublet and Hα, respectively, and also for the closest spherical and non-rotating CMFGEN model

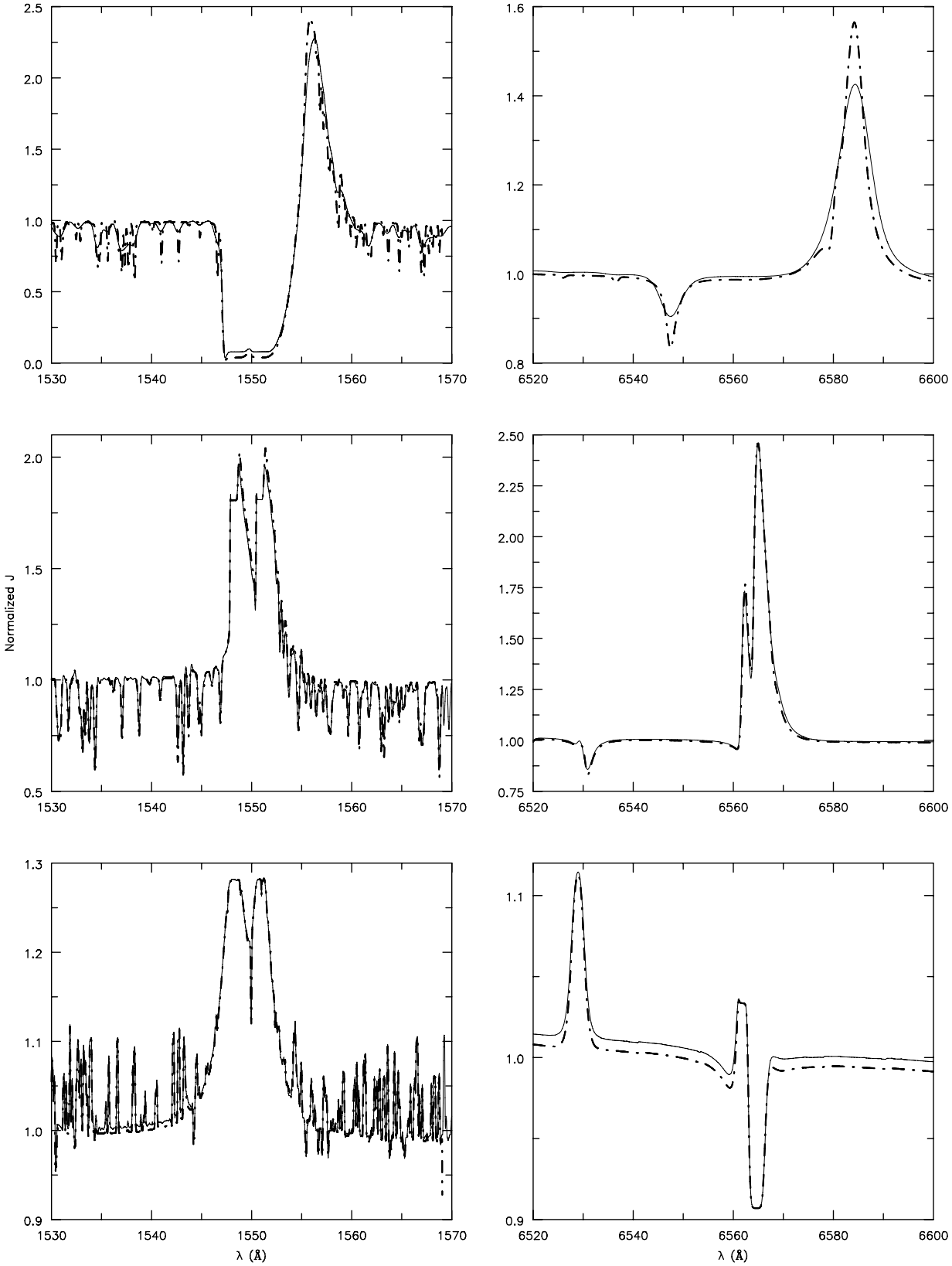

Fig. 7. The normalized J moment as a function of wavelength around the C IV $\lambda\lambda$1548–1552 doublet (*left column*) and Hα (*right column*) at different locations in the envelope of AV 83 (the stellar model is described in Table 1). The top row of figures shows J at $v_r \sim v_\infty$, the middle at $v_r \sim 0.1v_\infty$, while the bottom row displays J in the hydrostatic atmosphere ($v_r \sim 0$). Note, that all spectra are in the co-moving frame. The solid (thin) and dash-dotted (thick) lines were calculated by CMFGEN and our code, respectively. Even though this model is spherical, our code treated it as a 2D case. As expected for spherical models, we calculated identical J moments for every latitude.

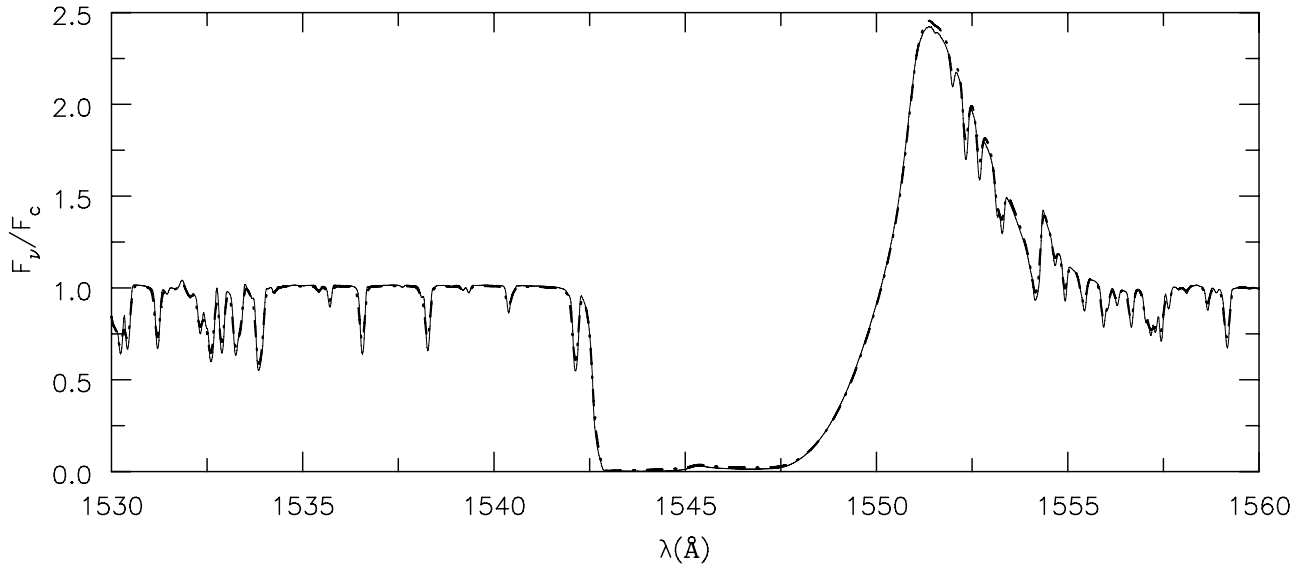

Fig. 8. The observed spectrum around the C IV $\lambda\lambda$1548–1552 doublet calculated by CMF_FLUX (thin solid line) and by our code (thick dash-dotted line). Note, that these spectra are in the observers' frame.

(thin/red line). It is obvious that substantial deviation occurs only in the outer envelope and only for photospheric lines. Strong P-Cygni profiles, like those of the C IV $\lambda\lambda$1548−1552 doublet, are barely affected apart from a little smoothing around the blue absorption edge and at the maximum emission. The Hα emission, on the other hand, changes its strength substantially between $\beta = 0$ and $\frac{\pi}{2}$. This sensitivity casts doubts about the reliability of Hα as an accurate mass loss indicator for rotating stars with unknown viewing angle. A similar sensitivity to the rotation can also be seen on the iron lines around C IV $\lambda\lambda$1548−1552 doublet that are also formed at the wind base.

Closer to the stellar surface the rotation effects on Hα diminish. At this depth, the behavior of narrow lines becomes interesting. The iron lines around C IV $\lambda\lambda$1548−1552 doublet are broadened and skewed to the blue. This is the combined result of the large angular size of the stellar surface, limb darkening, and the broken forward-backward symmetry in the azimuthal direction. We will discuss this issue below in detail. At stellar surface ($v_r \sim 0$) the optical depth is so large that any parcel of material sees only its immediate neighborhood which roughly moves with the same velocity. Consequently, no skewness, displacement or line-shape difference occurs between the profiles calculated for different latitudes (not shown in Figs. 9 and 10).

Figure 11 shows the detailed structure of the He I 4713.17 Å profile in J moment. Since this line is not affected by blending (see e.g., the second panel of Fig. 12), its position, shape, and width should clearly reflect the expected rotation effects and should highlight any inconsistencies in our model calculation. We present these profiles in velocity space and correct for the local radial velocities. The bottom row of Fig. 11 shows He I 4713.17 Å deep in the atmosphere ($v_r \sim 0$ and $\tau_\nu \gg 1$). The line is in weak emission centered around 0 km s^{-1} as expected. The profiles are similar at all latitudes which reflects the fact that only radiation from the nearby co-moving regions contributes to J at this position. The line width reflects the local turbulent velocity and temperature. The top row of Fig. 11 shows the normalized J at $v_r \sim V_\infty$. Here the line is in absorption and the profile widths show strong latitudinal dependence. We expect He I 4713.17 Å to form in the photosphere, far from the radii where $v_r \sim v_\infty$ ($r \sim 50 r_{\rm core}$). In the co-moving frame of this position the central star covers only a small solid angle on the sky and can be considered as moving away with a uniform velocity, roughly equal to v_∞. When we correct for the radial velocity of this position, we almost correctly account for the Doppler shift of each small section of the photosphere, hence, the profiles in Fig. 11 should be and are centered on ∼0 km s^{-1}. The polar view (solid line) shows the intrinsic line profile (unaffected by rotation) while the equatorial view (dash-dotted) broadened by ±250 km s^{-1} as it should.

The profiles displayed in the middle panel of Fig. 11 are more difficult to understand. They appear to be blueshifted and also skewed at $\beta = \frac{\pi}{4}$ and $\frac{\pi}{2}$. At these intermediate radii ($v_r \sim 0.1 v_\infty$ and $r \sim 1.5 r_{\rm core}$) the stellar surface covers a large portion of the sky and the Doppler shifts of photospheric regions vary substantially. The line profile in J is a superposition of the profiles emanating from different photospheric regions, and it is affected by the angular size of the photosphere and by the limb darkening. The line center should be redshifted by less than $0.1 v_\infty$ velocity which explains the ∼−20 km s^{-1} blueshift in the middle panel of Fig. 11 (i.e., we over compensated the Doppler shift). The blueward tilt of the profiles at $\beta = \frac{\pi}{4}$ and $\frac{\pi}{2}$ is caused by the forward-backward asymmetry around the rotational axis. The trailing and leading side of the photosphere contributes a broader and narrower profile, respectively, which causes the blueward tilt. We can conclude, therefore, that the gross characteristics of the He I 4713.17 Å line profiles in Fig. 11 reflect the expected features at all depths and reveal no inconsistencies in our method.

Figure 12 shows the observed spectra at different viewing angles around selected transitions. We also show the calculations of CMF_FLUX for the corresponding spherical model.

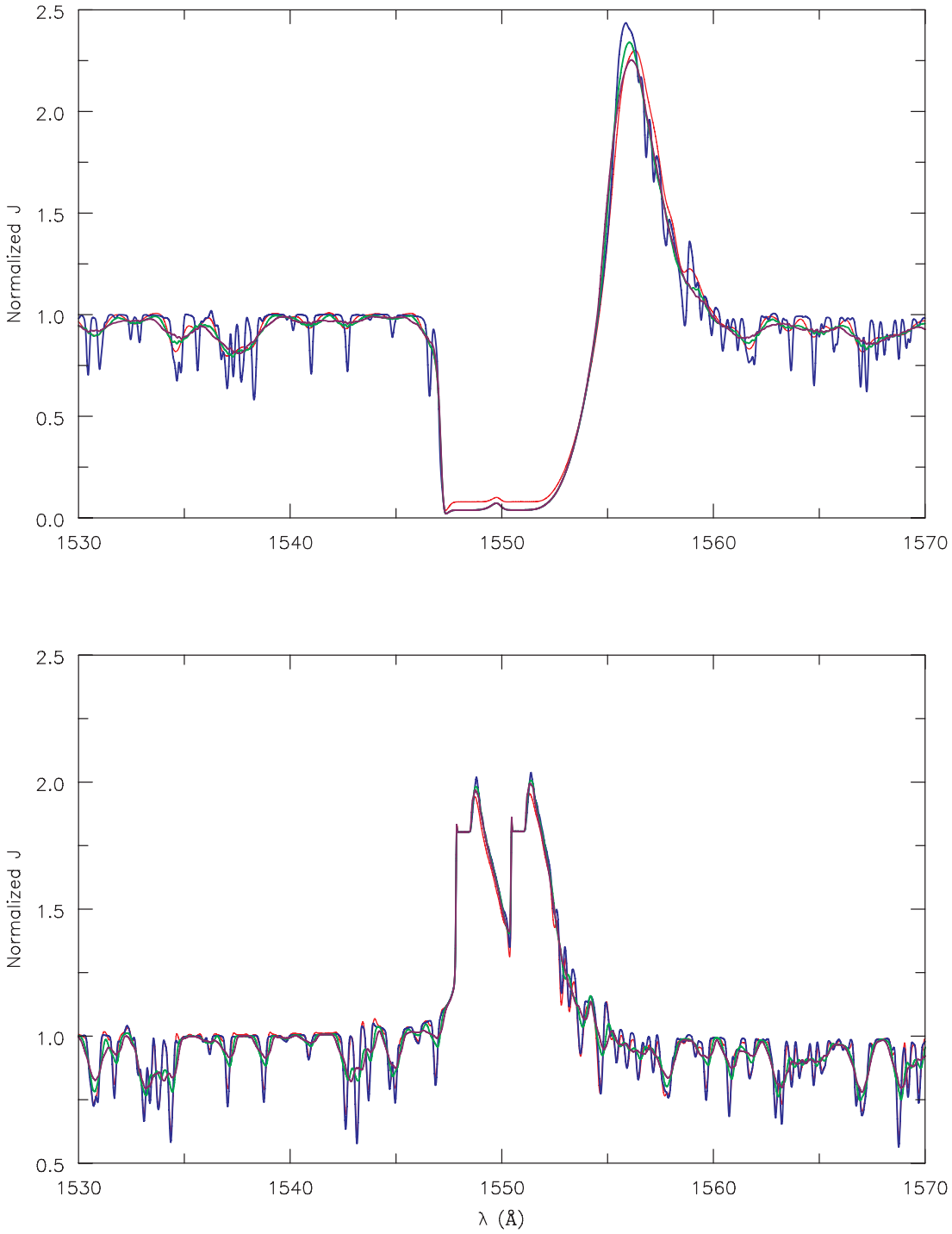

Fig. 9. The normalized J moment as a function of wavelength around the C IV $\lambda\lambda$1548–1552 doublet at $v_r \sim v_\infty$ (*top*) and at $v_r \sim 0.1v_\infty$ (*bottom*). The wind velocity is described by a simplified version of the WCD model, for which the polar velocities and the density enhancements were turned off (see text for description). The azimuthal rotation was calculated by Eq. (18) with $v_{\rm eq} = 250$ km s^{-1}. The thin (red) curve is the basic spherical symmetric model of AV 83 which was produced by CMF_FLUX. The thick blue, green, and purple lines were calculated by our code and display J for $\beta = 0$, $\frac{\pi}{4}$, and $\frac{\pi}{2}$, respectively.

Not surprisingly, the observed spectra reveal the same characteristics as those of J moment at large radii. For our purposes, the most important feature of Figs. 12 is the remarkable similarity to Figs. 4 and 5 of Busche & Hillier (2005). Despite the limited ability of our code to produce observed spectra, Fig. 12 shows all the qualitative features of the synthetic observations. Most of the differences are due to our treatment of the ES. Our code does not redistribute the scattered radiation in frequency space which would produce smoother features like those of Busche & Hillier (2005). Note, that we run CMF_FLUX with coherent ES for proper comparison; therefore, the spherical symmetric spectra also show sharper features.

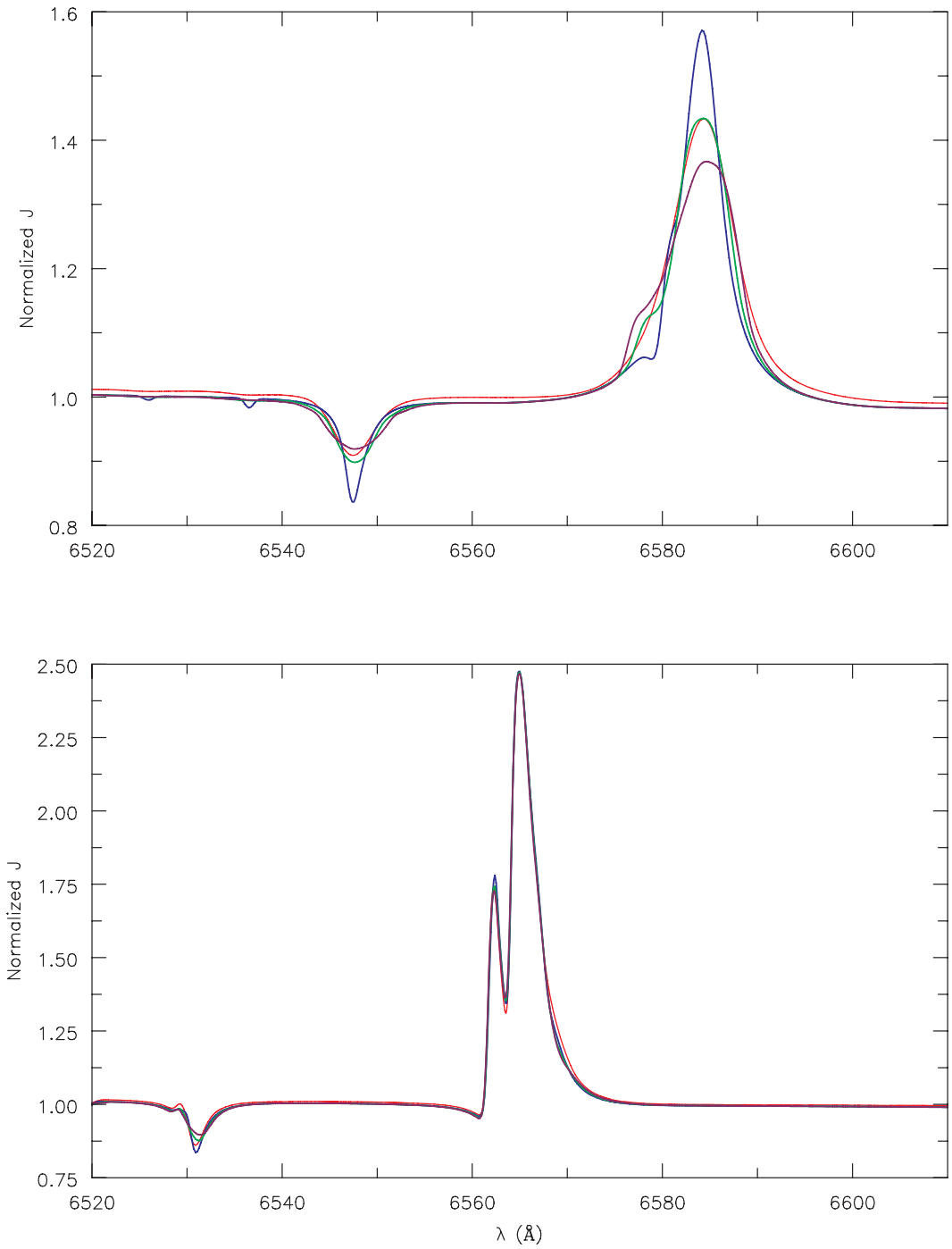

Fig. 10. Same as Fig. 9, but for the spectra around Hα.

4. Summary

We have implemented the short-characteristic method into a radiation transfer code that can handle axi-symmetric stellar models with realistic wind-flow velocities. This routine will replace the continuum transfer plus Sobolev approximation approach that is currently used in our axi-symmetric stellar atmosphere program (ASTAROTH, Paper I). The new transfer code allows for non-monotonic wind-flow and, therefore, will enhance ASTAROTH's ability to treat line transfer accurately in models for Be stars, OB rotators, binaries with colliding winds or accretion disks, pre-main sequence and young stars, and for collapsing core (Type-II) supernovae.

The most important improvements of our approach are the sampling method that we introduced to map the directional variation of the radiation, and the flexible approach to allow for non-monotonic velocity fields. We use a global grid in impact-parameters and in inclination angles (the angle between the equator and the plane containing the ray and the origin), and solve the transfer independently for every pair of these parameters. The code calculates the incoming intensities for the characteristics – a necessary feature of the short-characteristic

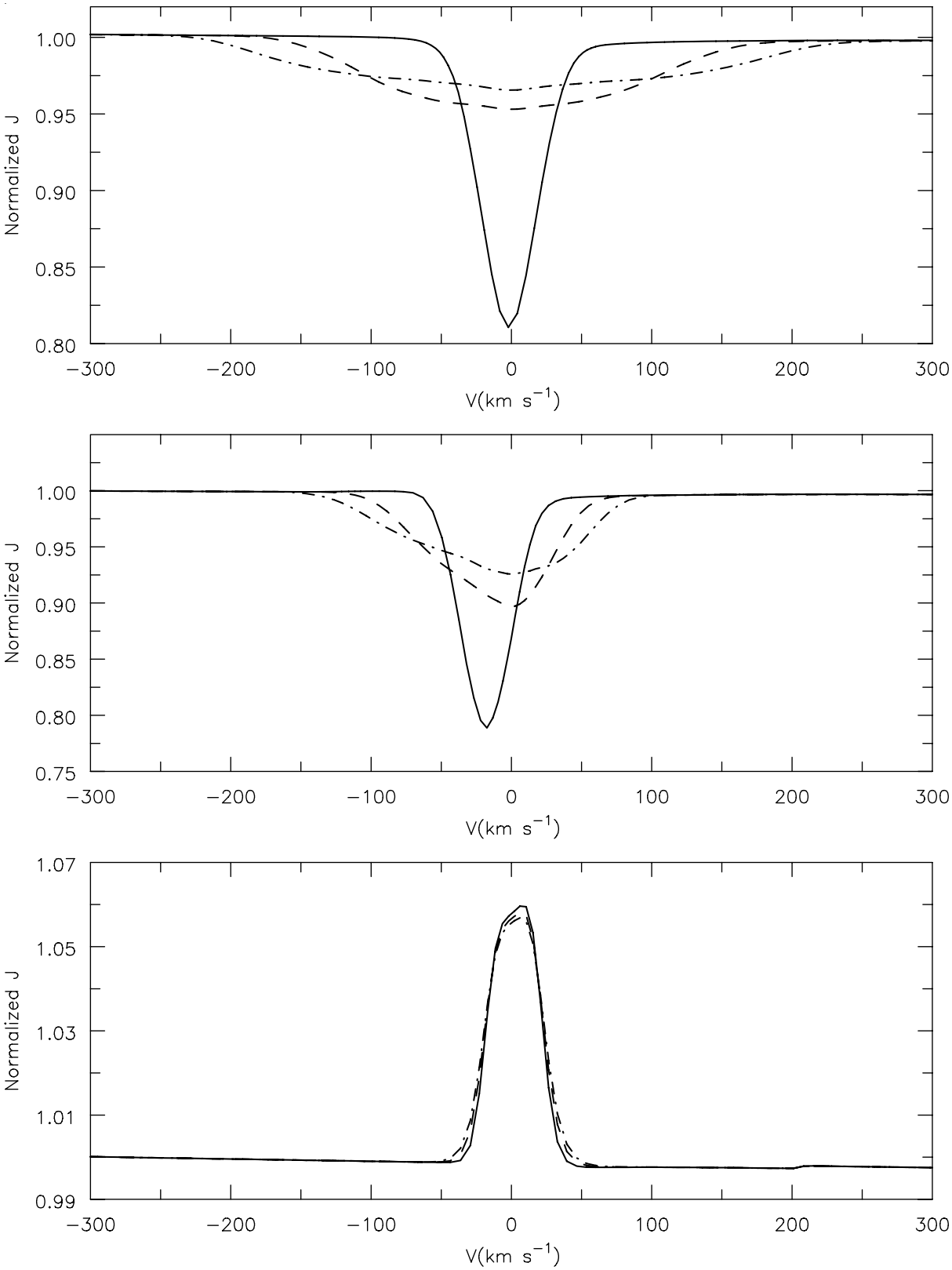

Fig. 11. Normalized J profiles of He I λ4713.17 at $v_r \sim v_\infty$ (*top*), $0.1v_\infty$ (*middle*), and 0 (*bottom*). The solid, dashed, and dash-dotted spectra are for $\beta = 0$ (pole), $\frac{\pi}{4}$, and $\frac{\pi}{2}$ (equator), respectively. The velocity scale is centered on the line and corrected for the above radial velocities. Our code reproduces the expected characteristics of the profiles within the uncertainties of our calculations (~20 km s^{-1}). Note the skewed line profiles at intermediate radii (*middle panel*) which are the results of the broken forward-backward symmetry around the rotational axis (see Sect. 3.3 for details).

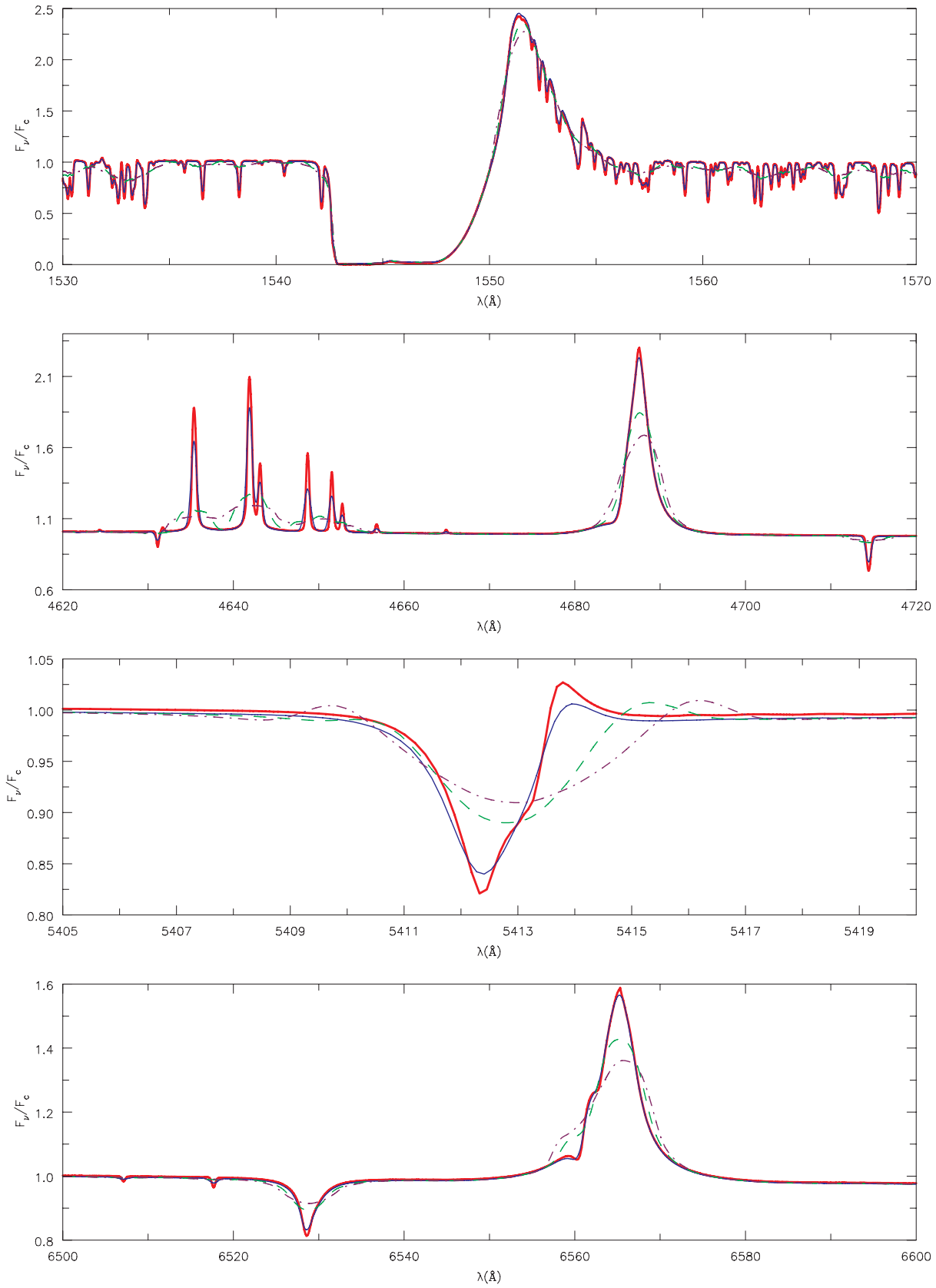

Fig. 12. The observed spectra of AV 83 around the C IV $\lambda\lambda$1548–1552 doublet (*top*), the C III/N III/He II emission complex between 4630−4700 Å, He II λ5411, and Hα (*bottom*), respectively. See Sect. 3.3 and Fig. 9 for the description of the model parameters. The thick (red) curve is the spherical model calculated by CMF_FLUX, while the thin (blue), dashed (green), and dashed-dotted (purple) curves are our calculations for viewing angles 0, $\frac{\pi}{4}$, and $\frac{\pi}{2}$, respectively. Note that the characteristics of these spectra (e.g., line widths and shapes) are very similar to those of Busche & Hillier (2005, see text for further details).

method – by a single latitudinal interpolation. Our approach eliminates the need for further interpolations in the radiation angles. The effects of the wind-flow are taken into account by adapting the resolution along the characteristics to the gradient of the flow velocity. This method ensures the proper frequency mapping of the opacities and emissivities where it is needed, but avoids performing unnecessary work elsewhere. Furthermore, it also provides flexibility in trading accuracy for speed.

The code also allows for distributed calculations. The work-load can be shared between the processors by either distributing the impact-parameter – inclination angle pairs for which the transfer is calculated or by assigning different frequency ranges to the processors.

We tested our code on static 1D/2D pure scattering problems. In all cases, it reproduced the reference result with an error of a few percent. More complex tests on realistic stellar envelopes, with and without rotation, were also performed. Our code reproduced the results of a well-tested 1D code (CMFGEN, Hillier & Miller 1998), as well as the expected features in 2D rotating atmospheres. These tests demonstrated the feasibility and accuracy of our method. In a subsequent paper, we will describe the implementation of our code into ASTAROTH and present the results of fully self-consistent 2D simulations.

Acknowledgements. This research was supported by NSF grant AST-9987390.

Appendix A: Interpolation methods

A.1. Linear interpolations

We used bi-linear interpolations to calculate opacity, source function, and line of sight velocity at non-grid positions in our modeling domain. The values were calculated by a weighted average of the corresponding quantities at the nearest grid points by

$$\chi(\nu) = \sum_{l=1}^{4} w_l \cdot \chi_l(\nu), \tag{A.1}$$

$$S(\nu) = \sum_{l=1}^{4} w_l \cdot S_l(\nu), \tag{A.2}$$

and

$$\underline{\boldsymbol{n}} \cdot \boldsymbol{v} = \sum_{l=1}^{4} w_l \cdot \left(\underline{\boldsymbol{n}} \cdot \boldsymbol{v}_l\right). \tag{A.3}$$

The nearest grid points are described as $l = 1$ (r_1, β_1), $l = 2$ (r_1, β_2), $l = 3$ (r_2, β_1), $l = 4$ (r_2, β_2); which set the weights in Eqs. (A.1)–(A.3) to

$$w_1 = \frac{r - r_2}{r_1 - r_2} \cdot \frac{\beta - \beta_2}{\beta_1 - \beta_2} \quad w_2 = \frac{r - r_2}{r_1 - r_2} \cdot \frac{\beta - \beta_1}{\beta_2 - \beta_1} \tag{A.4}$$

$$w_3 = \frac{r - r_1}{r_2 - r_1} \cdot \frac{\beta - \beta_2}{\beta_1 - \beta_2} \quad w_4 = \frac{r - r_1}{r_2 - r_1} \cdot \frac{\beta - \beta_1}{\beta_2 - \beta_1}. \tag{A.5}$$

Coordinates r $(r_2 \geq r > r_1)$ and β $(\beta_2 \geq \beta > \beta_1)$ are the coordinates of the general (non-grid) position. Note, that the frequency dependent quantities were interpolated in the co-moving frame!

Since the integrals in Eqs. (4) and (5) are evaluated in the co-moving frame of the down-stream end point of the characteristic, the opacities and source functions calculated by Eqs. (A.1) and (A.2) need to be properly Doppler corrected for the evaluation of the integrals. For a frequency ν in the co-moving frame of the down-stream end point the procedure goes as follows: a) first we find the Doppler shifts Δz_j by Eq. (A.3) for every integration point j on the characteristics (see Sect. 2.1 for definitions); b) we find co-moving frequencies ν_k and ν_{k-1} so that

$$\nu_k \geq \nu \cdot \left(1 - \Delta z_j\right) > \nu_{k-1} \tag{A.6}$$

at all integration points; c) we find the opacity and source function for ν_k and ν_{k-1} by Eqs. (A.1) and (A.2); d) we use linear interpolation in frequency space to get these parameters at $\nu \cdot \left(1 - \Delta z_j\right)$ for the integrations.

This seemingly cumbersome procedure is actually a straightforward book-keeping that can be programmed very efficiently in the presence of monotonic velocity fields. Note, that we do not mean global monotonicity but a velocity field that is monotonic along the SC! One can assure such a situation by properly creating the spatial grid.

A.2. Interpolation of the intensities

Linear interpolations of the intensities at the upstream end point of the SC does not provide acceptable accuracy. This is because of the accumulation of errors from all previous intensity interpolations. Extensive testing of our method showed that the best result was achieved by using monotonic cubic interpolations (e.g., Steffen 1990). We use this method to interpolate the intensities in β angle for fixed r and ν. The monotonic cubic approximation provides the necessary 3rd order accuracy, yet avoids artificial variations ("ringing") that can be amplified and propagated on our grid. Using monotonic interpolations actually dampens out such "ringings" and stabilizes our method.

An unfortunate effect of requiring monotonicity, however, is that we need to save the intensities for all frequencies and β angles on the previously treated shell (see Sect. 3 for description of our code). Fortunately, this does not impede our efforts to accommodate multi-processor calculations because all (p, i) pairs can still be treated independently. Only, we require an additional memory area for $\sim N_\beta N_\nu$ real number per (p, i) pair.

References

Auer, L. H., & Mihalas, D. 1972, ApJS, 24, 193
Auer, L. H., & Mihalas, D. 1973, ApJS, 25, 433
Bjorkman, J. E., & Cassinelli, J. P. 1993, ApJ, 409, 429
Brown, J. C., & McLean, I. S. 1977, A&A, 57, 141
Busche, J. R. 2001, Radiation Transfer in Axially Symmetric Systems, Ph.D. Thesis, University of Pittsburgh
Busche, J. R., & Hillier, D. J. 2000, ApJ, 531, 1071
Busche, J. R., & Hillier, D. J. 2005, AJ, 129, 454

Cassinelli, J. P., Brown, J. C., Maheswaran, M., Miller, N. A., & Telfer D. C. 2002, ApJ, 578, 951
Castor, J., Abbott, D. C., & Klein, R. I. 1975, ApJ, 195, 157
Crowther, P. A., Hillier, D. J., Evans, C. J., et al. 2002, ApJ, 579, 774
Dessart, L., & Hillier, D. J. 2005, A&A, 439, 671
Dessart, L., & Hillier, D. J. 2005, A&A, 437, 667
Georgiev L. N., Hillier, D. J., & Zsargó, J. 2005, in preparation (Paper I)
Gräfener, G., Koesterke, L., & Hamann, W.-R. 2002, A&A, 387, 244
Hauschildt, P. H., Baron, E., Starrfield, S., & Allard, F. 1996, ApJ, 462, 386
Herrero, A., Puls, J., & Najarro, F. 2002, A&A, 396, 949
Hillier, D. J. 1994, A&A, 289, 492
Hillier, D. J. 1996, A&A, 308, 521
Hillier, D. J., & Miller, D. L. 1998, ApJ, 496, 407
Hillier, D. J., Lanz, T., Heap, S. R., et al. 2003, ApJ, 588, 1039
Hubeny, I. 1992, in The Atmospheres of Early-Type Stars, ed. U. Heber, & C. J. Jeffery (Berlin: Springer), 377
Hubeny, I., & Lanz, T. 1995, ApJ, 439, 875
Jones, H. P. 1973, ApJ, 185, 183
Jones, H. P., & Skumanich, A. 1973, ApJ, 185, 167
Kifonidis, K., Plewa, T., Janka, H.-Th., & Müller, E. 2003, A&A, 408, 621
Kunasz, P. B., & Auer, L. H. 1988, J. Quant. Spectrosc. Radiat. Transfer, 39, 67
Kurucz, R. L. 1991, in Stellar Atmospheres: Beyond Classical Models, NATO ASI series C, V341, ed. L. Crivellari, I. Hubeny, & D. G. Hummer (Dordrecht: Kluwer), 441
Lucy, L. B. 2003, A&A, 403, 261
Lucy, L. B. 2002, A&A, 384, 725
Lucy, L. B. 1999, A&A, 344, 282
Maeder, A., & Meynet, G. 2000, A&A, 361, 159
Martins, F., Schaerer, D., & Hillier, D. J. 2002, A&A, 382, 999
Mihalas, D., Auer, L. H., & Mihalas, B. W. 1978, ApJ, 220, 1001
Ng, K. C. 1974, J. Chem. Phys., 61, 2680
Owocki, S. P., & ud-Doula, A. 2004, ApJ, 600, 1004
Owocki, S. P., Cranmer, S. R., & Gayley, K. G. 1996, ApJ, 472, L115
Pauldrach, A. W. A., Hoffmann, T. L., & Lennon, M. 2001, A&A, 375, 161
Petrenz, P., & Puls, J. 1996, A&A, 312, 195
Poeckert, R., & Marlborough, J. M. 1978a, ApJ, 220, 940
Poeckert, R., & Marlborough, J. M. 1978b, ApJS, 38, 229
Quirrenbach, A., Bjorkman, K. S., Bjorkman, J. E., et al. 1997, ApJ, 479, 477
Rybicki, G. B., & Hummer, D. G. 1991, A&A, 245, 171
Stee, Ph., de Araújo, F. X., Vakili, F., et al. 1995, A&A, 300, 219
Steffen, M. 1990, A&A, 239, 443
ud-Doula, A., & Owocki, S. P. 2002, ApJ, 576, 413
Wang, L., Howell, D. A., Höflich, P., & Wheeler, J. C. 2001, ApJ, 550, 1030